Optimized Gore/Seam Cable-Actuated Shape Control of Gossamer Membrane Reflectors

H. A. DeSmidt*
University of Tennessee, Knoxville, Tennessssee 37996

K. W. Wang†
Pennsylvania State University, University Park, Pennsylvania 16802

and

H. Fang‡
Jet Propulsion Laboratory, California Institute of Technology, Pasadena, California 91109

This investigation explores the feasibility of using an active gore/seam cable-based control system to reduce global root mean square figure errors due to thermal loading and inflation effects (W error) in large, gossamer, inflatable membrane reflectors. Analysis is performed on an inflated spherical membrane with polyvinylidene-fluoride-actuated radial cables, for which the cable lengths and attachment points are designed via genetic algorithm optimization. It is found that through proper tailoring of the cable lengths, significant global root mean square figure-error reduction is achieved. Specifically, root mean square errors due to on-orbit thermal loading were reduced by approximately 75% with a 104-cable active gore/seam cable-control system that has a mass equal to 15% the original reflector. Similarly, W errors were reduced by approximately 95% with a 104-gore/seam cable-control system with a mass ratio of 12%. Finally, to deal with simultaneous W error and thermal loading with uncertain relative magnitudes, a hybrid gore/seam cable-control configuration based on a combination of independently optimized thermal and W-error cable patterns is considered. By adjusting the weights of a hybrid objective function, the gore/seam cable-control system demonstrated robust shape-control performance for combined loading conditions. Because of the relatively lightweight designs and shape-control effectiveness, the gore/seam cable-shape-control concept seems promising for future gossamer reflector applications.

I. Introduction

ULTRALIGHTWEIGHT, deployable, inflatable membrane reflectors are attractive for space applications of optical mirrors and radio frequency antennas because they allow for large apertures, enabling the potential for both improved signal-to-noise and increased signal resolution. Typically, inflatable membrane reflectors consist of two circular membranes that are sealed on their edges, attached to a rim structure, and internally pressurized to produce a desired doubly curved surface (see Fig. 1). Thus, far, inflated lenticular reflectors have only been used for applications in which low imaging acuity is sufficient. However, one drawback that prohibits their use for high-precision applications is the difficulty in controlling and maintaining their shape to the desired spherical or parabolic profile [1].

Two main sources of figure error that occur in inflatable membrane reflectors arise from inflation and thermal effects. Specifically, upon inflation of a perfectly fabricated circular membrane, the structure forms a so-called Hencky surface, which deviates from the spherical and parabolic profiles [2–4]. This deviation is termed "W error," given by its shape. In addition to W error, another significant source of on-orbit figure error is due to thermal expansion and contraction of the reflector due to solar heating and Earth shadowing effects throughout the orbital period. Reflectors in orbit will experience both

bulk temperature shifts and thermal gradients across the structure [5]. Thus, to take full advantage of the potential benefits offered by inflatable membrane reflectors, some type of on-orbit shape-control treatment is necessary.

Previously, [6] investigated full-coverage-area polyvinylidene fluoride (PVDF) piezoelectric thin films for shape control of large (14-m) inflatable membrane reflectors. Here, it was shown that higher-order asymmetric figure errors due to manufacturing-tolerance-induced thickness and modulus variations could be sufficiently controlled. On the other hand, it was also found that PVDF films did not have sufficient authority to adequately control the low-order focal-length aberrations. Reference [7] investigated the optimal placement of PVDF patch actuators to control vibration of inflatable torus structures. Here, it was shown that the addition of thin PVDF patches did not significantly alter the modal characteristics of the inflated host structure. Reference [8] investigated a noncontact distributed actuation methodology of PVDF films using a steerable electron beam. Furthermore, [1] explored the performance of electron-beam-actuated electroactive polymers (EAP) for global shape control of the W error. Further, [9] explored the use of prescribed temperature deviations of various locations on a reflector to implement shape correction. Using this approach, RMS figure error due to a 20 K on-orbit bulk temperature shift was reduced by approximately 50%. Still, other researchers investigated boundary-actuation techniques (boundary control), in which the reflector rim or outer radial locations are actuated to adjust the overall shape [10–12]. Here, boundary control was effective in correcting higher-order disturbances such as astigmatism and comma, associated with uneven boundary stresses and mounting errors. Finally, others have proposed and studied various cable-actuated shape-control strategies. Reference [13] used tip-mast cable-tension adjustments on a tension-truss mesh antenna to compensate for temperature-induced figure errors. Similar to [9], the control was able correct the temperature-induced RMS figure errors by about 50%. Additionally, [14] explored the use of actively controlled gore/seam cables as a means of correcting the local

---

*Assistant Professor of Aerospace Engineering, Mechanical, Aerospace and Biomedical Engineering Department.
†William E. Diefenderfer Chaired Professor in Mechanical Engineering, Department of Mechanical and Nuclear Engineering.
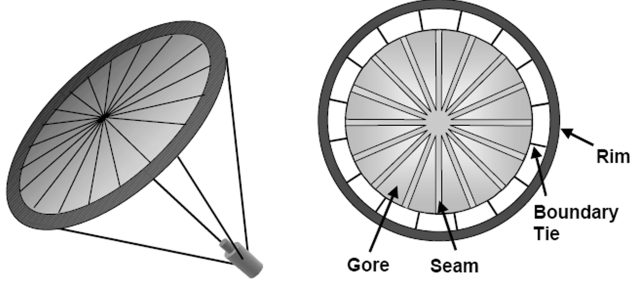‡Research Engineer.

Fig. 1 Inflatable membrane reflector with radial gore/seam construction.

Fig. 2 Reflector structural model: spherical membrane cap with prestress due to inflation.

curvature errors induced by the presence of seams in long-duration balloon structures. Further, [15] proposed the concept of PVDF-actuated seams for shape refinement of shape memory alloy (SMA) deployable "umbrella-type" reflectors. Here, it was shown that active piezoelectric PVDF tape placed along the seams could compensate for deployment errors resulting from gore/seam stiffness mismatches and SMA-wire temperature perturbations. Finally, [16] explored the use of active boundary web cables for vibration isolation of membranes from support-structure disturbances. Here, the active vibration-isolation strategy was enhanced through use of a double-layer perimeter cable configuration with passively tuned mass and stiffness properties to enable a vibration-absorption effect that reduced transmissibility between support and membrane.

Compared with full-coverage-area, directly actuated control configurations, the gore/seam control approach could offer weight saving benefits for membrane reflectors. This is especially the case for large-aperture (greater than 20-m) membrane reflectors, which favor the use of gores and seams in the manufacturing process [15]. However, the previous gore/seam control investigations focused mainly on correcting surface defects in the vicinity of the seams due to stiffness and deployment effects. To advance the state of the art, the goal of this investigation is to assess the feasibility of using an active gore/seam as a global shape controller to correct for other important sources of figure error in membrane reflectors. Specifically, this research develops and evaluates an externally reacted gore/seam cable-control system for correcting figure errors due to membrane-reflector on-orbit temperature deviations, thermal gradients, and W error.

II. Membrane-Reflector Model

To facilitate design and analysis and assess the effectiveness of the gore/seam cable-control system, a structural model of a large, inflatable, spherical membrane reflector is developed.

Specifically, the reflector is modeled as a thin, shallow, spherical cap structure with simply supported boundary conditions and prestress due to internal inflation pressure [17]. Furthermore, the reflector material is considered to be isotropic Kapton®. In this study, an example reflector testbed with dimensions and properties shown in Fig. 2 and Table 1 is used to evaluate the shape-control concepts.

The total reflector strain energy U_{ref}, given by Eqs. (1a–1d), accounts for elastic deformation, membrane tension $T_p = PR/2$ due to inflation pressure P, and thermal expansion due to temperature distribution $T(r, \theta)$ about some nominal temperature T_{nom}.
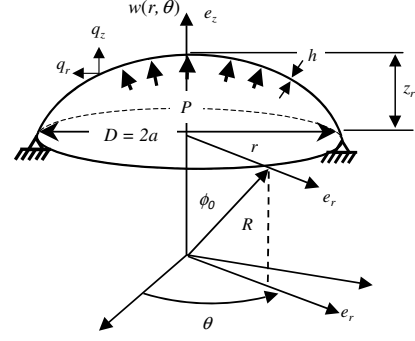
$$U_{\text{elastic}} = \int_0^{2\pi} \int_0^a \frac{1}{2} [N_{rr}\varepsilon_{rr} + N_{r\theta}\varepsilon_{r\theta} + N_{\theta\theta}\varepsilon_{\theta\theta}] r \, dr \, d\theta \quad (1a)$$

$$U_{\text{stretch}} = \int_0^{2\pi} \int_0^a \frac{T_p}{2} \left[\left(\frac{\partial w}{\partial r}\right)^2 + \left(\frac{1}{r}\frac{\partial w}{\partial \theta}\right)^2 \right] r \, dr \, d\theta \quad (1b)$$

$$U_{\text{therm}} = \int_0^{2\pi} \int_0^a \left[N_{rr}^T \varepsilon_{rr} + N_{r\theta}^T \varepsilon_{r\theta} + N_{\theta\theta}^T \varepsilon_{\theta\theta} \right] r \, dr \, d\theta \quad (1c)$$

$$U_{\text{ref}} = U_{\text{elastic}} + U_{\text{stretch}} + U_{\text{therm}} \quad (1d)$$

where the elastic stress resultants N_{rr}, $N_{r\theta}$, and $N_{\theta\theta}$ are given by

$$N_{rr} = K(\varepsilon_{rr} + \mu\varepsilon_{\theta\theta}), \qquad N_{\theta\theta} = K(\varepsilon_{\theta\theta} + \mu\varepsilon_{rr})$$
$$N_{r\theta} = (K/2)(1 - \mu)\varepsilon_{r\theta} \quad (2)$$

with $K = Eh/(1 - \mu^2)$, and the midplane strain-displacement relations are given by

$$\varepsilon_{rr} = \frac{\partial u}{\partial r} + \frac{w}{R} \qquad \varepsilon_{\theta\theta} = \frac{u}{r} + \frac{1}{r}\frac{\partial v}{\partial \theta} + \frac{w}{R} \qquad \varepsilon_{r\theta} = \frac{\partial v}{\partial r} - \frac{v}{r} + \frac{1}{r}\frac{\partial u}{\partial \theta} \quad (3)$$

Furthermore, the thermal stress resultants N_{rr}^T, $N_{r\theta}^T$, and $N_{\theta\theta}^T$ are given as

$$N_{rr}^T = -\frac{Eh}{1 - \mu}\alpha_{\text{CTE}}(T_{\text{nom}} - T)$$
$$N_{\theta\theta}^T = -\frac{Eh}{1 - \mu}\alpha_{\text{CTE}}(T_{\text{nom}} - T), \qquad N_{r\theta}^T = 0 \quad (4)$$

Finally, the work due to external loading is given as

$$W_{\text{load}} = \int_0^{2\pi} \int_0^a q_z(r, \theta) r \, dr \, d\theta \quad (5)$$

To perform analysis on the system, an assumed-mode Ritz method is used. Because the reflector is considered a shallow shell structure, the in-plane displacements are neglected (i.e., $u = 0$ and $v = 0$) and only the transverse deflection $w(r, \theta)$ is considered. Because of the circular planform and the fixed boundary conditions at the rim,

Table 1 Reflector dimensions and material properties

Reflector dimensions		Reflector material properties (Kapton)	
Radius of curvature	$R = 56$ m	Density	$\rho = 1420$ kg/m³
Planform diameter	$D = 35$ m	Elastic modulus	$E = 2.5$ GPA
Planform radius	$a = 17.5$ m	Poisson's ratio	$\mu = 0.34$
Center rise height	$z_r = 2.805$ m	Thermal expansion coefficient	$\alpha_{\text{CTE}} = 20$ ppm/K
Thickness	$h = 50$ μm	Yield stress	$\sigma_y = 172$ MPa

$w(r, \theta)$ is expanded in terms of a Fourier–Bessel series modal expansion with unknown coefficients W_{0_m}, $W_{c_{nm}}$, and $W_{s_{nm}}$:

$$w(r, \theta) = \sum_{m=1}^{N_m} W_{0_m} J_0(\lambda_{0m}r) + \sum_{n=1}^{N_n} \sum_{m=1}^{N_m} J_n(\lambda_{nm}r)[W_{c_{nm}} \cos(n\theta)$$
$$+ W_{s_{nm}} \sin(n\theta)] \tag{6}$$

where $J_n(\lambda_{nm}r)$ is a Bessel function of the first kind and λ_{nm} are the characteristic roots satisfying $J_n(\lambda_{nm}a) = 0$. Furthermore, the Fourier-Bessel series expansion order used throughout this investigation is $N_n = 12$ and $N_m = 12$.

III.   Figure Errors and Loading Conditions

To assess feasibility and performance of the gore/seam shape-control strategy on the large inflatable membrane reflector, this investigation considers two sources of figure error that require on-orbit shape correction. The first such error is the so-called W error that is inherent to inflated lenticular structures. The second source of figure error considered is due to thermal expansion and thermal gradients caused by solar heating and Earth shadowing throughout the orbit cycle.

A.   W Error

The reflector is considered to be a near-net-shaped spherical reflector that, before inflation, has a nonzero central rise height $w_0(0) = z_0 < z_r$. Specifically, the initial (uninflated) reflector profile $w_0(r)$ and radius of curvature R_0 are

$$w_0(r) = \sqrt{R_0^2 - r^2} - \sqrt{R_0^2 - a^2} \tag{7}$$

with

$$R_0 = \frac{z_0^2 + a^2}{2z_0}$$

and the desired reflector profile is

$$w_r(r) = \sqrt{R^2 - r^2} - \sqrt{R^2 - a^2} \tag{8}$$

with

$$R = \frac{z_r^2 + a^2}{2z_r}$$

Inflation pressure is required to achieve the desired central rise height, $z_r = 2.805$ m. However it is well known that inflation does not preserve the spherical profile and hence is the source of the so-called W error.

In this investigation, the W error is calculated based on results from Jenkins and Marker [4], which considers large nonlinear deflections due to inflation of an initially flat circular membrane to some final rise height. Here, the so-called Hencky theory is used to approximate the W error due to inflation from the initial central rise height z_0, to the desired central rise height, $z_r = 2.805$ m (Fig. 3). The resulting inflated reflector profile $w_{\text{inf}}(r)$ with $w_{\text{inf}}(0) = z_r$ is given as

$$w_{\text{inf}}(r) = w_0(r) + (z_r - z_0)\left[1 + \frac{a_2}{a_0}\left(\frac{r}{a}\right)^2 + \frac{a_4}{a_0}\left(\frac{r}{a}\right)^4 + \frac{a_6}{a_0}\left(\frac{r}{a}\right)^6 \right.$$
$$\left. + \frac{a_8}{a_0}\left(\frac{r}{a}\right)^8 + \cdots \right] \tag{9a}$$

with

$$b_0 = 1.724, \quad a_0 = 0.653, \quad a_2 = \frac{-1}{b_0}, \quad a_4 = \frac{-1}{2b_0^4}, \quad a_6 = \frac{-5}{9b_0^7}$$

$$a_8 = \frac{-55}{72b_0^{10}}, \cdots \tag{9b}$$

The resulting W error is given as $\Delta w_{\text{W error}}(r) = w_r(r) - w_{\text{inf}}(r)$ and shown in Fig. 3.

Finally, the inflation pressure P_0, required to achieve a desired central rise height z_r, is

$$P_0 = \left[\frac{z_r - z_0}{a_0 a}\right]^3 \frac{Eh}{a} \tag{10}$$

B.   Thermal Loading

To account for the thermal effects, both bulk temperature shifts T_0 about a nominal on-orbit temperature T_{nom} and linear temperature gradients ΔT across the reflector are investigated. Equation (11) gives the general form of the temperature distribution considered:

$$T(r, \theta) = T_{\text{nom}} + T_0 + \Delta T \frac{r}{2a} \cos(\theta) \tag{11}$$

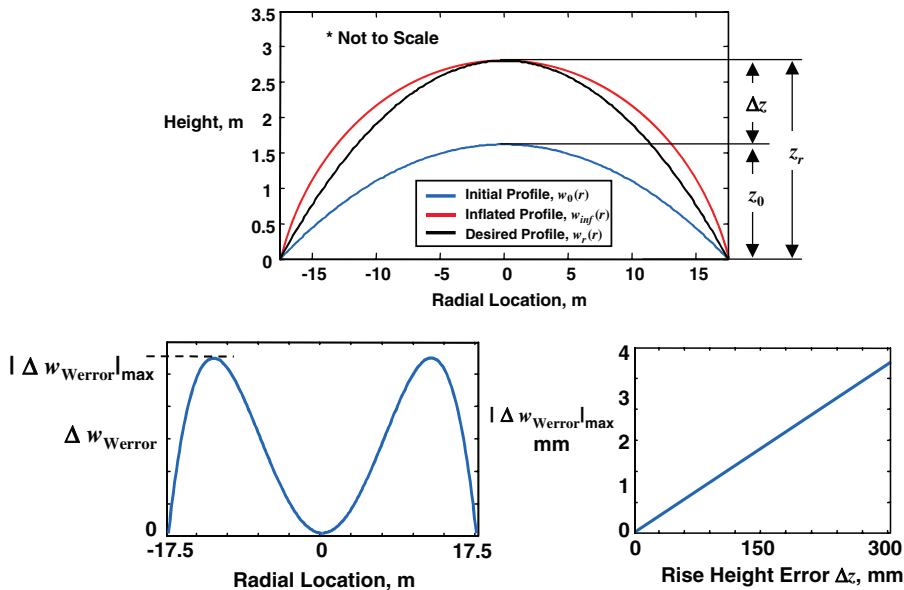For example, Fig. 4 shows the temperature distribution for a $\Delta T = 20$ K thermal gradient load.
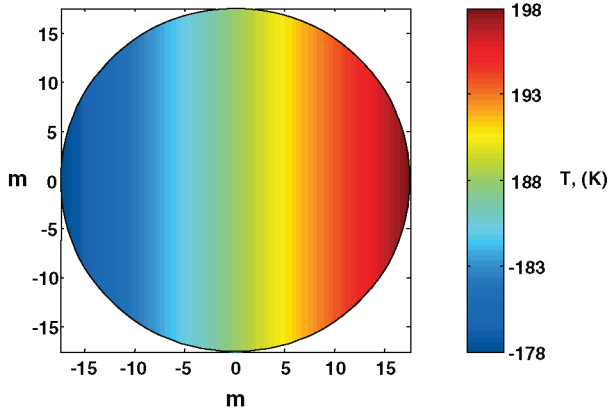

Fig. 3   W-error profile.

Fig. 4 Reflector temperature distribution for thermal gradient load, $\Delta T = 20$ K.

Table 2 Inflation and prestrain

Inflation pressure	$P = 14.52$ Pa
Membrane tension	$T_p = 408.1$ N/m

The resulting surface deflections produced by the bulk and gradient temperature deviations, T_0 and ΔT, must be continuously corrected via the on-orbit shape-control system because they vary throughout orbital position. However, to account for the net thermal contraction of the reflector due to the shift from Earth's nominal temperature $T_{\text{nom Earth}}$ to the on-orbit nominal temperature T_{nom}, additional inflation pressure P_{nom} is required:

$$P_{\text{nom}} = 2\alpha_{\text{CTE}}(T_{\text{nom Earth}} - T_{\text{nom}})\frac{Eh}{R(1 - \mu)} \qquad (12)$$

Thus, the total required inflation pressure is $P = P_0 + P_{\text{nom}}$. In this study, we will assume that $T_{\text{nom Earth}} = 293$ K (20°C) and $T_{\text{nom}} = 188$ K. Table 2 summarizes the inflation pressure and resulting membrane tension.

IV. Gore/Seam Cable Actuation

The actuation strategy explored in this study involves the use of cable actuators running along the existing gores/seams of the reflector. Specifically, pretensioned cables run radially along the reflector surface from an attachment point on the reflector and are connected to PVDF end actuators that adjust the cable tensions T_c, producing reflector shape adjustments (see Fig. 5).

The radial gore/seam cables are pretensioned due to membrane inflation and conform to reflector curvature. The cables are not bonded to the surface, except at the attachment point on one end of the cable. Thus, no shear stress is developed between the membrane and the cable, only normal stresses. The other end of the cable is connected to a PVDF actuator that is anchored to the fixed rim boundary. The PVDF actuator operates in the so-called d_{33} mode,
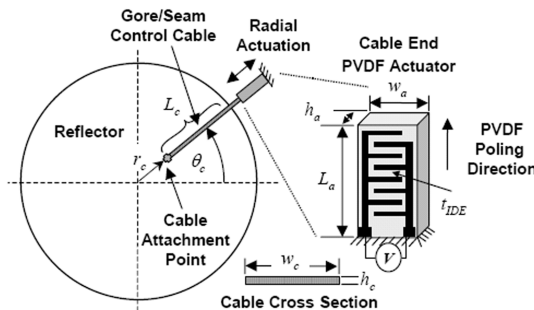
with control voltage V applied to an interdigitated electrode with finger spacing t_{IDE} [18,19].

In this investigation, N_c control cables are considered with uniform angular spacing, hence the angular position of the ith cable is given as

$$\theta_{c_i} = \frac{2\pi(i - 1)}{N_c} \qquad (13)$$

Furthermore, due to the spherical geometry of the reflector, the length of the ith cable L_{c_i} is related to the attachment point radial location r_{ci} by

$$L_{c_i} = R\left[\sin^{-1}\left(\frac{a}{R}\right) - \sin^{-1}\left(\frac{r_{ci}}{R}\right)\right] \qquad (14)$$

The attachment point locations r_{ci} are design variables determined using a genetic algorithm (GA) optimization to maximize the shape-control effectiveness for a given type of disturbance.

Because the cables run through the gores/seams of the reflector, the transverse deflection at a given point of the cable must be the same as that of the reflector. Thus, the total displacement d_{c_i} at the end of the ith cable is

$$d_{c_i} = \delta_{c_i} - \left[\int_{r_{c_i}}^a \frac{w(r, \theta_{c_i})}{R}\mathrm{d}r + w(r_{c_i}, \theta_{c_i})\frac{r_{c_i}}{R}\right] \qquad (15)$$

where δ_{c_i} is the elastic stretch of the ith cable. Also, the cable and end-actuator axial stiffness values, k_{c_i} and k_a, are given by Eq. (16) (see Fig. 6):

$$k_{c_i} = \frac{E_cA_c}{L_{c_i}}, \qquad k_a = \frac{E_aA_a}{L_a} \qquad (16)$$

with $A_c = w_ch_c$ and $A_a = w_ah_a$. Together with Eqs. (15) and (16), the strain energies of the radial cables and actuators are

$$U_{\text{cable}} = \frac{1}{2}\sum_{i=1}^{N_c}\frac{E_cA_c}{L_{c_i}}\delta_{c_i}^2$$

$$U_{\text{act}} = \frac{1}{2}\sum_{i=1}^{N_c}\frac{E_aA_a}{L_a}d_{c_i}^2 + \sum_{i=1}^{N_c}\frac{E_aA_ad_{11}}{t_{\text{IDE}}}d_{c_i}V_i \qquad (17)$$

Using the cable and end-actuator strain energies in Eq. (17) along with the reflector strain energy in Eq. (1), applying the Ritz method with the assumed displacement field in Eq. (6), and recognizing the additional cable elastic-stretch degrees of freedom δ_{c_i}, the system
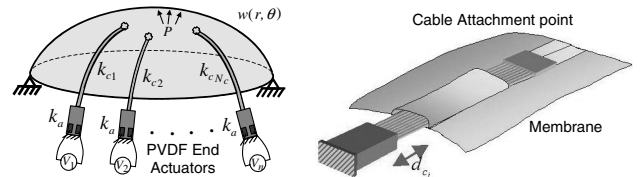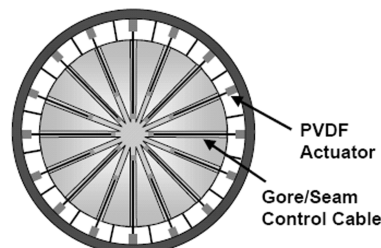

Fig. 6 Cables connected in series with end actuators.

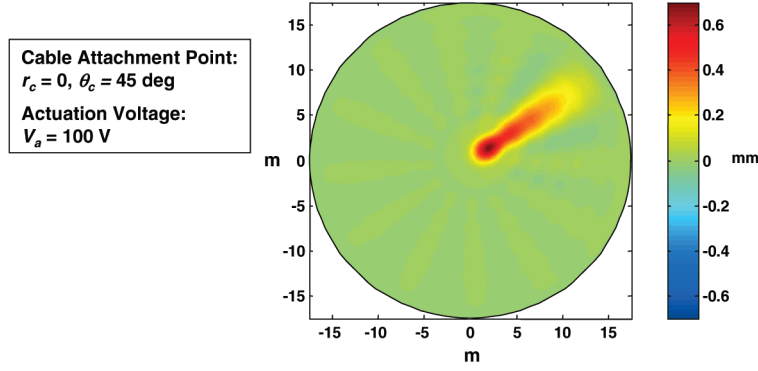**Fig. 5 PVDF-actuated radial gore/seam cables.**

Fig. 7   Reflector surface deformation produced by gore/seam cable actuator.

equations for the reflector with cable control become

$$\frac{\partial(U_{\mathrm{ref}} + U_{\mathrm{cable}} + U_{\mathrm{act}} - W_{\mathrm{load}})}{\partial X_i} = 0$$

$$\Rightarrow (K_{\mathrm{ref}} + K_{\mathrm{cable}} + K_{\mathrm{act}})X = F_{\mathrm{load}} + F_{\mathrm{therm}} + F_{\mathrm{act}} \quad (18)$$

where generalized coordinate vector $X = [W_{0_m} \cdots W_{c_{nm}} \cdots W_{s_{nm}} \cdots \mid \delta_{c_i} \cdots]^T$; K_{ref}, K_{cable}, and K_{act} are the stiffness matrices of the reflector, cables, and actuators, respectively; and F_{load}, F_{therm}, and F_{act} are the forces due to external loading, thermal effects, and the PVDF end actuators, respectively.

One important design consideration is the cable axial stiffness k_c. Because the end actuators operate in series with the cable to actuate the reflector, k_c must be large enough to effectively transmit actuator forces without exceeding actuator stroke limitations. In other words, if k_c is too low, then the end actuator may "run out" of stroke before achieving the desired level of actuation force on the reflector.

To aid in the cable design, the stroke attenuation factor γ from the actuator to the reflector is defined as

$$\gamma = \frac{1}{1 + k_r/k_c} \quad (19)$$

where $k_r = 1/\delta_r$, $0 < \gamma \le 1$, and δ_r is the unit-load influence coefficient of the reflector at the cable attachment point. Because the cable is confined to run along the reflector midsurface within the gore/seam, the thickness of the cable h_c is constrained to be less than the reflector thickness h (i.e., $h_c < h = 50~\mu\mathrm{m}$). Furthermore, because cable length L_c is determined by GA optimization to maximize modal controllability, the only parameters available to design the cable axial stiffness are the cable width w_a and cable material. In this investigation, the cables are designed such that $\gamma > 0.9$. Both the cable and PVDF cable end-actuator parameters used in this investigation are summarized in Table 3.

To avoid depoling of the PVDF actuators, the maximum allowable actuation voltage V_{max} is determined from the PVDF depoling field E_{max} and the interdigitated electrode spacing [19] as

$$V_{\mathrm{max}} = E_{\mathrm{max}} t_{\mathrm{IDE}} \quad (20)$$

Finally, Fig. 7 shows the reflector deformation produced by applying 100 V to a single radial cable actuator. This figure demonstrates that the gore/seam cable actuators primarily generate localized surface deformations distributed along the length of the cable, with the largest deformations occurring near the cable attachment point $r = r_c$.

V.   Shape-Control Law

In this investigation, the shape-control law is based on a weighted least-squares (LS) approach. The general form of the system is

$$K_{\mathrm{sys}} X = F_d + F_c \quad (21)$$

where K_{sys} is the system stiffness matrix, and F_d and F_c are generalized force vectors due to external disturbances and control inputs, respectively. Furthermore, $F_c = B_u U$, where U is a vector of control-input voltages for the cable end actuators and B_u is the corresponding control-input distribution matrix. By considering a vector $Y = C_y X$ of surface displacements measured from a rectangular grid of sensors, the transfer matrix representation of the system is written as

$$Y = T_{yu} U + Y_0 \quad (22)$$

where T_{yu} is the system transfer matrix ($T_{yu} = C_y K_{\mathrm{sys}}^{-1} B_u$), and Y_0 is a vector of sensor measurements of the uncontrolled reflector.

$$Y_0 = C_y K_{\mathrm{sys}}^{-1} F_d \quad (23)$$

Based on the sensor measurements and the transfer matrix, the least-squares shape-control law is

$$U = -\left[T_{yu}^T T_{yu} + w_{\mathrm{eff}} I\right]^{-1} T_{yu}^T Y_0 \quad (24)$$

which minimizes the following objective function in the least-squares sense:

$$J = Y^T Y + \alpha U^T U \quad (25)$$

where α is the control-effort weighting that is used as a design

Table 3   Cable and PVDF actuator properties

| End-actuator properties (PVDF)		Cable properties (carbon fiber)	
Density	$\rho_a = 1780~\mathrm{kg/m^3}$	Density	$\rho_c = 1750~\mathrm{kg/m^3}$
Elastic modulus	$E_a = 2.27~\mathrm{GPA}$	Elastic modulus	$E_c = 207~\mathrm{GPA}$
Poisson's ratio	$\mu_a = 0.225$	Poisson's ratio	$\mu_c = 0.3$
Thickness	$h_a = 500~\mu\mathrm{m}$	Thickness	$h_c = 50~\mu\mathrm{m}$
Width	$w_a = 204~\mathrm{mm}$	Width	$w_c = 50~\mathrm{mm}$
Length	$L_a = 408~\mathrm{mm}$		
Piezoelectric constants	$d_{11} = 21 \times 10^{-12}~\mathrm{m/V}$		
Depoling electric field	$E_{\mathrm{max}} = 30 \times 10^6~\mathrm{V/m}$		
Interdigitated electrode spacing	$t_{\mathrm{IDE}} = 25~\mu\mathrm{m}$		
Maximum allowable voltage	$V_{\mathrm{max}} = 750~\mathrm{V}$		
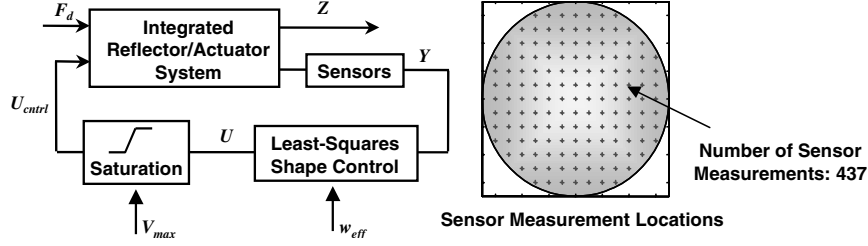
Fig. 8   Least-squares shape-control system.

parameter to adjust the amount of control effort exerted on the reflector by the control system.

Because the PVDF material has a maximum allowable control-voltage magnitude, $V_{\max}$, which must not be exceeded to avoid depoling the actuator, the control input U is passed through a saturation block that clips any control voltages with magnitudes exceeding $V_{\max}$. The overall schematic of the control system is shown in Fig. 8.

VI.   Optimization and Shape-Control Results

In this section, the shape-control performance of the externally reacted gore/seam cable-control configuration described in Sec. IV combined with the LS shape-control law in Sec. V is investigated under the loading conditions described in Sec. III. The shape-control performance is assessed in terms of RMS figure error w_{RMS}:

$$w_{\mathrm{RMS}} = \sqrt{\frac{1}{\pi a^2} \int_0^a \int_0^{2\pi} w(r, \theta)^2 r\,\mathrm{d}\theta\,\mathrm{d}r} \qquad (26)$$

The gore/seam cable-length optimization methodology is summarized in Fig. 9.

Figure 10 shows the $N_c = 52$ and $N_c = 104$ cable-pattern designs obtained from GA optimization of the cable length for the uniform thermal loading case and the W-error disturbance case. Here, in the W-error case, it is seen that the optimization scheme places all of the control-cable attachment points near the W-error maximum-deflection location. Thus, the control cables are relatively short, which results in less added mass and increased cable axial stiffness (better stroke attenuation factor γ). However, this phenomenon does not occur for the uniform thermal load case, in which the maximum deflection is at the center. In this case, the optimized cable lengths vary significantly with angular location, resulting in a larger distribution of cable attachment locations. Physically, this is due to the fact that the maximum deflection due to the each gore/seam cable occurs at its attachment point (see Fig. 7). Therefore, the optimization staggers the attachment locations to prevent large localized deflections, which otherwise would reduce surface precision. The performance of the resulting optimized designs are summarized in Table 4.
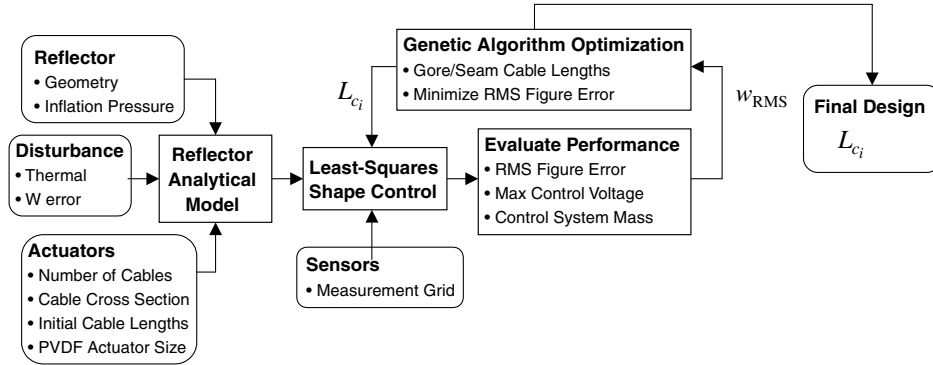

Fig. 9   Genetic algorithm cable-length optimization for maximum figure-error reduction.
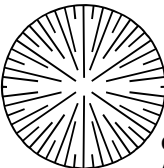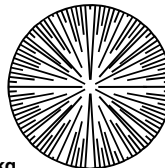
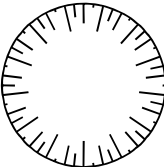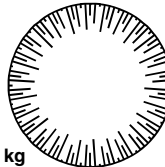Fig. 10   Genetic algorithm optimized cable configurations for gore/seam cable-actuated shape control.

Table 4   Optimized gore/seam cable-actuated shape-control performance

| Cable pattern	Cable and actuator mass, kg	Loading condition	Initial RMS error, mm	Residual RMS error, mm	RMS reduction, %	Max actuator voltage, V	Max actuator stroke, mm
52-cable thermal	5.68	$T_0 = 15$ K	4.754	1.421	70.1	750.0[a]	0.518
		$\Delta T = 30$ K	2.069	0.890	57.5	374.7	0.457
104-cable thermal	11.08	$T_0 = 15$ K	4.754	0.856	82.1	543.1	0.173
		$\Delta T = 30$ K	2.069	0.641	69.4	508.9	0.135
52-cable W error	4.60	$|w|_{max} = 3.0$ mm	2.185	0.197	91.1	417.8	0.064
104-cable W error	9.24	$|w|_{max} = 3.0$ mm	2.185	0.109	95.2	254.7	0.038

[a]Saturated.

Figures 11 and 12 show the reflector surface deflections and cable end-actuator control voltages for a 15 K uniform temperature deviation and a 30 K temperature gradient disturbance, respectively. Figure 13 shows the surface deformations and voltages for W-error disturbance with $|w|_{max} = 3.0$ mm.

Figure 14 shows the percent of RMS figure-error reduction versus the external disturbance magnitudes. Initially, the percent of RMS reduction remains constant; however, for disturbance magnitudes beyond a certain level, the percent of reduction begins to decrease. This is a result of voltage saturation of the PVDF end actuators. Figure 14 demonstrates that in each disturbance case, both the unsaturated and saturated RMS reduction performance is improved on the order of ∼10 to 20% by doubling the number of cable actuators from 52 to 104. Furthermore, for a given cable configuration, the disturbance level at which saturation begins can be

increased by increasing the end-actuator cross-sectional area, resulting in a tradeoff between actuator mass and RMS performance.

To address the issue of combined thermal and W-error disturbance conditions, a hybrid cable configuration based on the GA optimized thermal and W-error cable designs is introduced. When optimizing for individual loading (i.e., pure thermal load or pure W error), the disturbance magnitude is not important because it does not affect the resulting shape (due to linearity). Thus, only the load distribution is needed to perform the cable-length optimization for the pure loading cases. However, in the case of simultaneous loads, the relative loading magnitudes of the individual loading mechanisms affect the overall shape. Because the relative magnitude between the W error and thermal loads is not constant due to on-orbit temperature variations, optimization for a specific W-error/thermal-load combination is not beneficial, as with the pure W error or pure
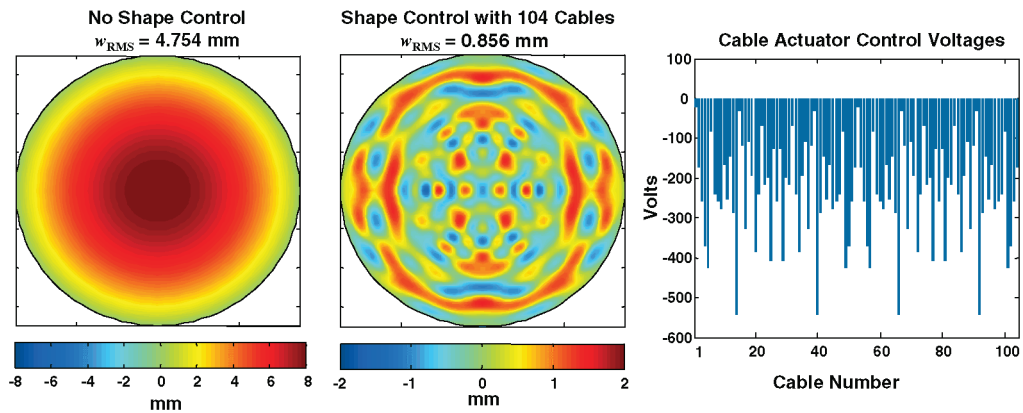
Fig. 11   Reflector surface deformations due to uniform temperature shift, $T_0 = 15$ K.
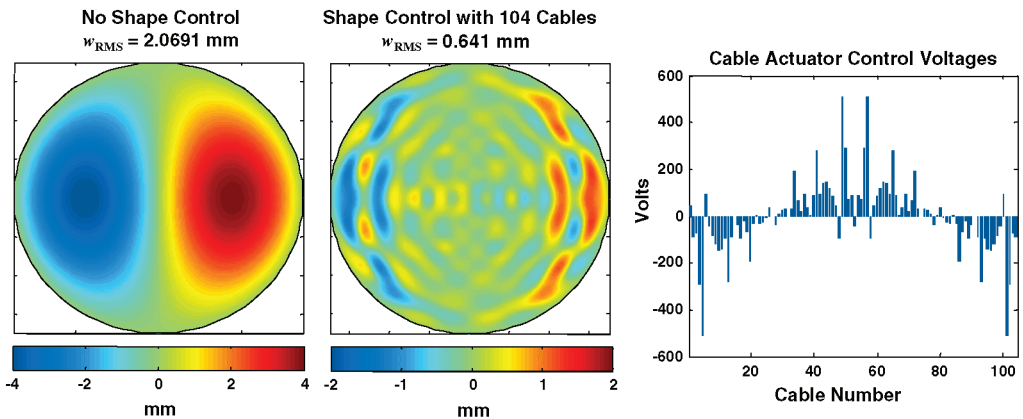
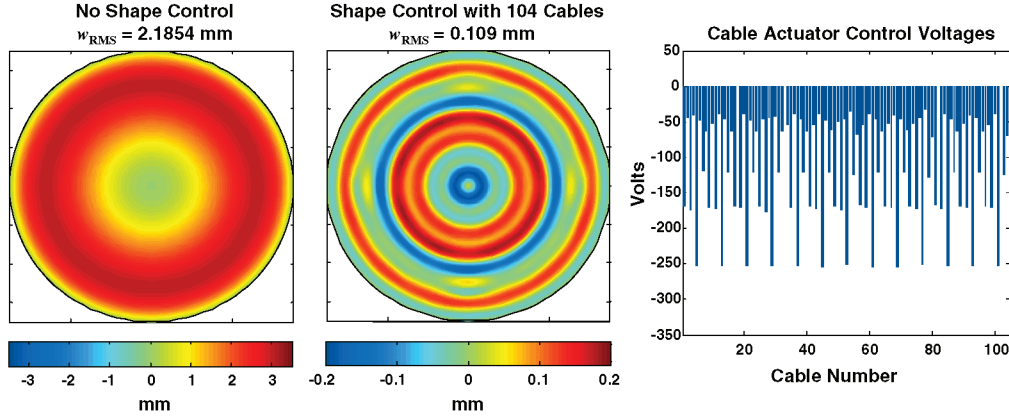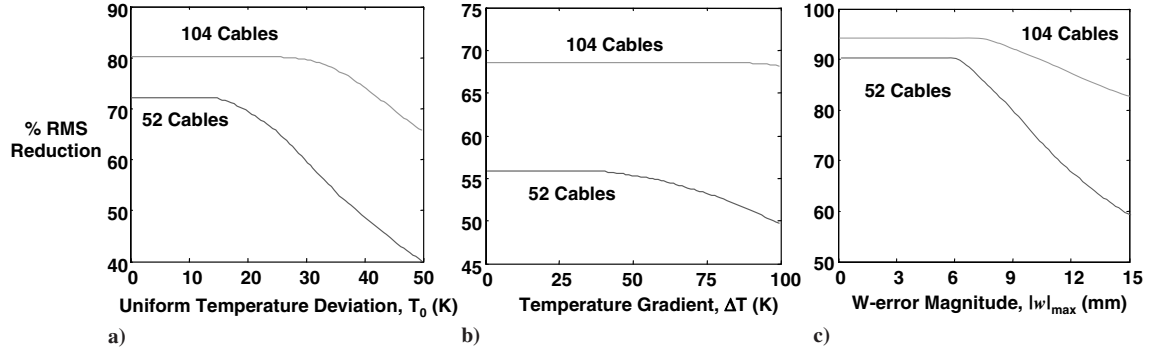Fig. 12   Reflector surface deformations due to temperature gradient, $\Delta T = 30$ K.

Fig. 13   Reflector surface deformations due to W error, $|w|_{max} = 3.0$ mm.

Fig. 14   Percent RMS error reduction vs disturbance magnitude; GA optimized cable configuration: a–b) thermal design and c) W-error design.
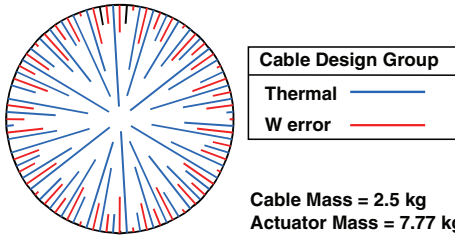

Fig. 15   Hybrid 52-cable thermal and 52-cable W-error configuration.

thermal load cases. Therefore, a hybrid cable configuration is considered that is a combination of the separately optimized W error and thermal designs. Specifically, Fig. 15 shows the hybrid 104-cable configuration, consisting of cables from the 52-cable thermal design alternated with cables from the 52-cable W-error design.

By adjusting the relative control-effort weight parameters α_{therm} and $\alpha_{W\,error}$ of the thermal and W-error cable-control voltages U_{therm} and $U_{W\,error}$ in the hybrid objective function J_{hybrid}, the RMS figure-

error performance of the shape-control law is maximized for a particular combined loading condition.

$$J_{hybrid} = Y^T Y + \alpha_{therm} U_{therm}^T U_{therm} + \alpha_{W\,error} U_{W\,error}^T U_{W\,error} \quad (27)$$

Figure 16 compares the RMS figure-error performance of each cable configuration under various combined thermal and W-error loading conditions. This analysis demonstrates that under pure thermal loading conditions ($T_0 \neq 0$, $\Delta T \neq 0$, and $|w|_{max} = 0$), the thermal cable designs achieve the best RMS shape-control performance; likewise, under pure W-error loading ($T_0 = 0$, $\Delta T = 0$, $|w|_{max} \neq 0$), the W-error designs achieve the best performance.

However, the hybrid design outperforms both the thermal and W-error designs for mixed loading conditions and achieves significant performance for pure W-error and pure thermal loading. Thus, from a robustness standpoint, the hybrid configuration is the best overall design choice.

Finally, Fig. 17 shows the effect of reflector membrane tension T_p on the gore/seam cable-actuated shape-control performance for various loading conditions. Here, T_p is varied from 0 to 2000 N/m,
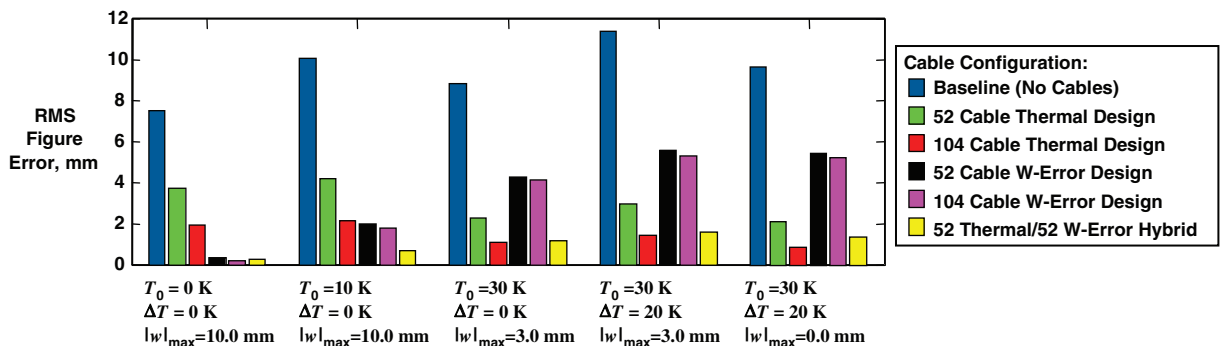

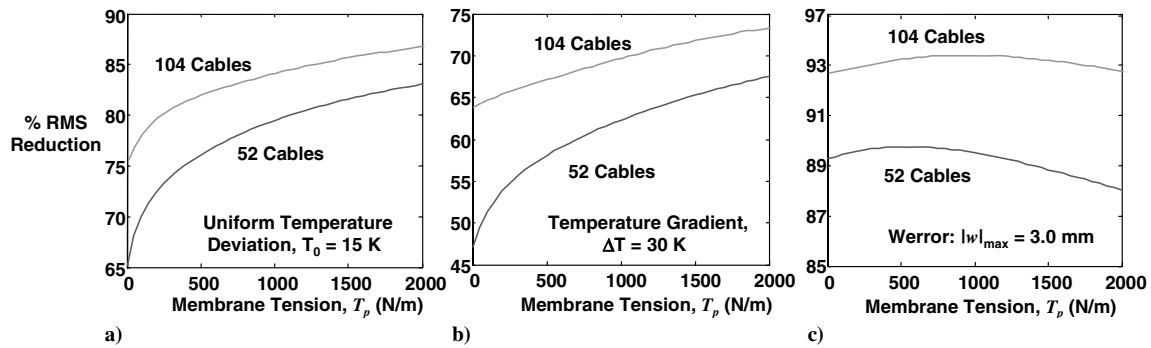**Fig. 16   Combined loading performance comparison.**

Fig. 17   Percent RMS figure-error reduction vs reflector membrane tension; GA optimized cable configuration: a–b) thermal design and c) W-error design.

where $T_p = 2000$ N/m corresponds to a membrane stress of approximately 25% of the Kapton yield stress. In the thermal gore/seam cable configuration, increasing membrane tension improves the shape-control effectiveness for both uniform and gradient thermal loads. In the W-error gore/seam cable configuration, the system is less sensitive to reflector membrane tension effects, however, there is an optimum value of T_p that maximizes the gore/seam cable W-error shape-control performance.

VII.   Conclusions

This investigation explored the feasibility of using an active gore/seam cable configuration to reduce global RMS figure errors due to thermal loading and inflation effects (W error) in large gossamer inflatable reflectors mounted on a rigid rim structure. It was found that through proper tailoring of cable lengths and attachment points, significant global RMS figure-error reduction is achieved. Specifically, in the cases studied, RMS errors due to thermal loading can be reduced by approximately 75% with a 104-cable active gore/seam cable-control system that has a mass of approximately 15% of the original reflector membrane. Similarly, W errors can be reduced by approximately 95% with a 104-cable active gore/seam cable-control system with a mass ratio of 12%. To effectively to deal with simultaneous W-error and thermal loading conditions, a hybrid gore/seam cable configuration based on a combination of the GA optimized thermal and W-error cable patterns was investigated. The hybrid cable configuration achieved significant RMS reduction of pure thermal- and W-error-induced disturbances, as well as for combined loading conditions, and had a mass ratio of approximately 14%; therefore, the hybrid configuration had the most robust performance. Finally, it was observed that reflector membrane tension had a significant impact on the gore/seam shape-control effectiveness when correcting thermally induced figure errors. Specifically, increasing reflector membrane tension improved the percent of RMS reduction performance by approximately 20%.

Because of the relatively lightweight designs and shape-control effectiveness, the gore/seam cable-based shape-control concept is promising for further development and application on gossamer membrane reflectors. The present analysis considers the case of a membrane mounted on a rigid rim structure, however, one important aspect to explore in future studies is the effect of rim compliance due to various rim-structure designs. Because the gore/seam cable actuators are anchored to the rim, in-plane rim compliance will be an important design consideration when using gore/seam cable actuators.

References

[1] Bao, X., Bar-Cohen, Y., Chang, Z., Sherrit, S., and Badescu, M., "Wirelessly Controllable Inflated Electroactive Polymer (EAP) Reflectors," *Smart Structures and Materials 2005: Electroactive Polymer Actuators and Devices (EAPAD)*, Vol. 5759-52, International Society for Optical Engineering (SPIE), San Diego, CA, 2005.
[2] Hencky, H., "Über den Spannungszustand in Kreisrunden Platten," *Zeitschrift für Mathematik und Physik*, Vol. 63, 1915, pp. 311–317.
[3] Campbell, J. D., "On the Theory of Initially Tensioned Circular Membranes Subjected to Uniform Pressure," *Quarterly Journal of Mechanics and Applied Mathematics*, Vol. 9, 1956, pp. 84–93.
[4] Jenkins, C. H., and Marker, D. K., "Surface Precision of Inflatable Membrane Reflectors," *Journal of Solar Energy Engineering*, Vol. 120, No. 4, Nov. 1998, pp. 298–305.
[5] Jenkins, C. H., and Faisal, S. M., "Thermal Load Effects on Precision Membranes," *Journal of Spacecraft and Rockets*, Vol. 38, No. 2, Mar.–Apr. 2001, pp. 207–211.
[6] Salama, M., Kuo, C. P., Garba, J., and Wada, B., "On-Orbit Shape Correction of Inflatable Structures" AIAA Paper 1994-1771, 1994.
[7] Lewis, J. A., and Inman, D. J., "Finite Element Modeling and Active Control of an Inflated Torus Using Piezoelectric Devices," *Journal of Intelligent Material Systems and Structures*, Vol. 12, No. 12, Dec. 2001, pp. 819–833.
[8] Martin, J. W., Redmond, J. M., Barney, B. S., Henson, T. D., Wehlburg, J. C., and Main, J. A., "Distributed Sensing and Shape Control of Piezoelectric Bimorph Mirrors," *Journal of Intelligent Material Systems and Structures*, Vol. 11, No. 10, Oct. 2000, pp. 744–757.
[9] Haftka, R. T., and Adelman, H. M., "An Analytical Investigation of Shape Control of Large Space Structures by Applied Temperatures," *AIAA Journal*, Vol. 23, No. 3, Mar. 1985, pp. 450–457.
[10] Jenkins, C. H., Wilkes, J. M., and Marker, D. K., "Improved Surface Accuracy of Precision Membrane Reflectors Through Adaptive Rim Control," AIAA Paper AIAA-98-1983, 1998.
[11] Lindler, J. E., and Flint, E. M., "Boundary Actuation Shape Control Strategies for Thin Film Single Surface Shells," 45th AIAA/ASME/ASCE/AHS/ASC Structures, Structural Dynamics and Materials Conference, Palm Springs, CA, AIAA Paper 2004-1825, 2004.
[12] Patrick, B., Moore, J., Chodimella, S., Maji, A., Marker, D., and Wilkes, M., "Meter-Class Membrane Mirror with Active Boundary Control," 46th AIAA/ASME/ASCE/AHS/ASC Structures, Structural Dynamics and Materials Conference, Austin, TX, AIAA Paper 2005-1825, 2005.
[13] Tabata, M., and Natori, M. C., "Active Shape Control of a Deployable Space Antenna Reflector," *Sixth International Conference on Adaptive Structures*, Technomic, Lancaster, PA, Nov. 1995, pp. 177–187.
[14] Jenkins, C. H., and Schur, W. W., "Gore/Seam Architectures for Gossamer Structures," *Journal of Spacecraft and Rockets*, Vol. 39, No. 5, Sept.–Oct. 2002, pp. 669–673.
[15] Duvvuru, H., Hossain, A., and Jenkins, C. H., "Modeling of an Active Seam Antenna," 44th AIAA/ASME/ASCE/AHS/ASC Structures, Structural Dynamics and Materials Conference, Norfolk, VA, AIAA Paper 2003-1739, 2003.
[16] Sakamoto, H., and Park, K. C., "Advanced Cable Boundary Layer Design in Membrane Structures for Dynamic Wrinkle Reduction," 46th AIAA/ASME/ASCE/AHS/ASC Structures, Structural Dynamics and Materials Conference, Austin, TX, AIAA Paper 2005-1973, 2005.
[17] Soedel, W., *Vibrations of Shells and Plates*, Marcel Dekker, New York, 1986.
[18] Gu, H., and Wang, M. L., "Interdigitated PVDF Transducer for Flaw Detection," *Proceedings of SPIE*, Vol. 6174, Apr. 2006, pp. 47–57.
[19] Bent, A. A., and Hagood, N. W., "Piezoelectric Fiber Composites with Interdigitated Electrodes," *Journal of Intelligent Material Systems and Structures*, Vol. 8, No. 11, Nov. 1997, pp. 903–919.